Metallic species, oxygen and silicon in the lunar exosphere: Upper limits and prospects for LADEE measurements

Menelaos Sarantos,[1,2,3] Rosemary M. Killen,[3,4] David A. Glenar,[3,5,6] Mehdi Benna,[7] and Timothy J. Stubbs[3,7,8]

Received 29 July 2011; revised 20 December 2011; accepted 22 December 2011; published 13 March 2012.

[1] The only species that have been so far detected in the lunar exosphere are Na, K, Ar, and He. However, models for the production and loss of species derived from the lunar regolith through micrometeoroid impact vaporization, sputtering, and photon-stimulated desorption, predict that a host of other species should exist in the lunar exosphere. Assuming that loss processes are limited to ballistic escape, photoionization, and recycling to the surface, we have computed column abundances and compared them to published upper limits for the Moon. Only for Ca do modeled abundances clearly exceed the available measurements. This result suggests the relevance of some loss processes that were not included in the model, such as the possibility of gas-to-solid phase condensation during micrometeoroid impacts or the formation of stable metallic oxides. Our simulations and the recalculation of efficiencies for resonant light scattering show that models for other species studied are not well constrained by existing measurements. This fact underlines the need for improved remote and in situ measurements of the lunar exosphere such as those planned by the Lunar Atmosphere and Dust Environment Explorer (LADEE) spacecraft. Our simulations of the LADEE neutral mass spectrometer and visible/ultraviolet spectrometer indicate that LADEE measurements promise to provide definitive observations or set stringent upper limits for all regolith-driven exospheric species. We predict that observations by LADEE will constrain assumed model parameters for the exosphere of the Moon.

Citation: Sarantos, M., R. M. Killen, D. A. Glenar, M. Benna, and T. J. Stubbs (2012), Metallic species, oxygen and silicon in the lunar exosphere: Upper limits and prospects for LADEE measurements, *J. Geophys. Res.*, *117*, A03103, doi:10.1029/2011JA017044.

1. Introduction

[2] Our Moon is the nearest to Earth example of a Surface Bounded Exosphere (SBE). To date, only four constituents from this collisionless atmosphere have been positively identified: Ar and He that were detected in situ by the neutral mass spectrometer deployed on the lunar surface by Apollo 17, and Na and K that were detected by ground-based observations in the late 1980s and have been extensively studied since (see review by *Stern* [1999]). Many more species of regolith origin are expected to populate the lunar exosphere given the presence of neutrals such as O, Ca, and Mg in the similar exospheric environment of Mercury [e.g., *Killen et al.*, 2007; *McClintock et al.*, 2009]. Pickup ions from the Moon, such as O^+, Si^+, Na^+ and Al^+, were measured by the AMPTE and WIND spacecraft [*Hilchenbach et al.*, 1992; *Mall et al.*, 1998]. And more recently, He^+, C^+, O^+, Na^+, K^+, and Ar^+ were observed above the Moon by the ion mass spectrometer onboard SELENE (Kaguya) [*Yokota et al.*, 2009; *Tanaka et al.*, 2009; *Saito et al.*, 2010]. It is still unclear whether these ions are primarily of exospheric origin and hence track exospheric abundances, or whether they contain nonnegligible fluxes of secondary ions sputtered directly from the surface [*Elphic et al.*, 1991].

[3] Several searches have so far failed to detect other neutral elements mainly due to the fact that, for many of the expected species, the strongest emission lines lie in the ultraviolet (UV) part of the spectrum that cannot be observed through the Earth's atmosphere. Nevertheless, published

[1]Heliophysics Science Division, NASA Goddard Space Flight Center, Greenbelt, Maryland, USA.
[2]Goddard Planetary Heliophysics Institute, University of Maryland, Baltimore County, Baltimore, Maryland, USA.
[3]NASA Lunar Science Institute, NASA Ames Research Center, Moffett Field, California, USA.
[4]Planetary Magnetospheres Branch, NASA Goddard Space Flight Center, Greenbelt, Maryland, USA.
[5]Astronomy Department, New Mexico State University, Las Cruces, New Mexico, USA.
[6]Emeritus, NASA Goddard Space Flight Center, Greenbelt, Maryland, USA.
[7]Solar System Exploration Division, NASA Goddard Space Flight Center, Greenbelt, Maryland, USA.
[8]Center for Research and Exploration in Space Science and Technology, University of Maryland, Baltimore County, Baltimore, Maryland, USA.

0148-0227/12/2011JA017044

upper limits show clearly a nonstoichiometry, or a disproportionality, between the exospheric and the surface abundances of numerous surface constituents [*Fastie et al.*, 1973; *Feldman and Morrison*, 1991; *Flynn and Stern*, 1996; *Stern et al.*, 1997]. Alkalis are particularly enhanced in the exosphere. Possible reasons for this trend are (1) that Na and K are promoted to the gas phase through processes more efficient than other metals, (2) that losses for other metals are more efficient than ballistic escape and photoionization would suggest, or (3) both of the above.

[4] Regolith-derived atoms in the lunar exosphere, the focus of this paper, originate during the bombardment of the surface by solar photons, solar wind ions and micrometeoroids. These processes were reviewed for Mercury by *Killen et al.* [2007] and *Domingue et al.* [2007]. For alkalis, such as sodium and potassium, the incident solar UV photons are energetic enough to release atoms in a process termed photon-stimulated desorption (PSD) [*Madey et al.*, 1998; *Yakshinskiy and Madey*, 1999]. For refractory elements, which are tightly bound in silicate phases, only energetic processes such as high-speed impacts and sputtering by the solar wind can provide the energy needed to break bonds. Consequently, the concentration of regolith-derived exospheric species reflects not only their relative surface abundance but also the ease with which they are liberated from the regolith. This is dependent on the micrometeoroid influx and speed, the amount of regolith vaporized, the average sputtering yield per incident solar wind ion (which is itself related to the composition of the solar wind), and other poorly constrained parameters. Loss processes also control the exospheric content; for instance, many lunar and hermean surface constituents may be promoted to the gas phase not only as atoms but also as molecular oxides [*Killen et al.*, 2005; *Killen et al.*, 2010; *Berezhnoy and Klumov*, 2008; *Berezhnoy*, 2010]. If the unknown dissociation lifetimes of molecules such as CaO, MgO, TiO are long, then the fraction of atomic neutrals that are bound in molecules will not be observed.

[5] The interplay between source and loss processes must be constrained by models and improved by additional observations and laboratory experiments. In these three aspects, sodium is by far the best studied species. Recently, *Sarantos et al.* [2010] included results from 20 years of ground-based sodium exosphere observations, and compared the observed sodium intensity to the prevailing UV and solar wind environment during the time of the observation. They found that the measured sodium intensity levels and their variation with phase angle were consistent with PSD. The inferred cross sections by *Sarantos et al.* [2010], $3 - 7 \times 10^{-21}$ cm^2, were somewhat smaller than laboratory-measured yields for PSD, $\sim 3 \times 10^{-20}$ cm^2 [*Yakshinskiy and Madey*, 1999], to compensate for expected losses inside the regolith [*Cassidy and Johnson*, 2005]. However, the exospheric sodium content was not constant over a lunation but increased by factors of 2–3 when the Moon was in the solar wind (high ion flux environment). The apparent solar wind control of the exospheric sodium could not be attributed to sputtering if sputtering yields typical of regolith surfaces are assumed (<0.1 atoms per ion impact). *Sarantos et al.* [2010] concluded that the solar wind ions enhance the desorption process by promoting the diffusion of sodium from regolith grains, or that they increase sodium levels by sputtering from heavy solar wind ions like He^{++}. Similar generation processes were inferred for Mercury's exospheric sodium in recent analyses of ground-based observations [e.g., *Mura et al.*, 2009; *Mouawad et al.*, 2011] and observations obtained by the Mercury Surface, Space Environment, Geochemistry, and Ranging (MESSENGER) spacecraft during its three flybys of the planet [*Burger et al.*, 2010]. In summary, the sources that create the lunar sodium population appear to be (in order of importance) (1) ion-augmented photon-stimulated desorption (PSD), (2) micrometeoroid impact vaporization, and (3) solar wind sputtering. How these results translate to the generation of other species remains speculative at the moment [e.g., *Morgan and Killen*, 1997; *Wurz et al.*, 2007; *Wurz et al.*, 2010].

[6] The characterization of the Moon's exosphere with measurements from orbit is a prime science objective of NASA's Lunar Atmosphere and Dust Environment Explorer (LADEE) mission. Planned for launch in 2013, LADEE will examine the lunar exosphere and dust environment with a payload that consists of a Neutral Mass Spectrometer (NMS), an Ultraviolet/Visible Spectrometer (UVS), and an in situ dust detector called the Lunar Dust Experiment (LDEX). The nominal mission lifetime is planned to be 100 days. While the exact orbit is still to be fully defined, we assume in this paper that it will be retrograde, equatorial, with periapse ~25 km above the dawn terminator and an apoapse ~75 km above the dusk terminator. The scientific objectives of the mission are to be achieved by measuring known species with spatial and temporal resolution sufficient to investigate the processes that control their distribution and variability, and by surveying a wide inventory of possible species to make new detections or to establish new upper limits [*Delory et al.*, 2009].

[7] To illuminate the existing measurements, help define expectations for the LADEE mission, and facilitate the interpretation of expected scientific results, we have carried out simulations of the production and loss of exospheric oxygen, silicon, and other metallic species. We have previously applied a model of exospheric particle transport to describe the source rates of the lunar sodium exosphere, and we validated it against ground-based observations [*Sarantos et al.*, 2010]. The model successfully described several key observables seen in sodium data: the overall intensity levels, the subsolar density of ~60–70 atoms cm^{-3}, and the increase in scale height from the subsolar region to the terminators and poles. In section 2 we extend this model to predict exospheric densities for O, Si, Fe, Al, Ti, Ca, Mg, K, and Mn, compare the model to published upper limits, and quantify the model uncertainties. In section 3 we estimate the constraints that the NMS measurements can place on the production of these species. In section 4 we examine the expected levels of resonant scattering emission from these species, and assess whether their detection is affected by the UVS instrument noise and zodiacal light. The paper concludes in section 5 with a summary of our results, which show that LADEE measurements can further our present understanding for many of the species studied because the expected signal-to-noise ratio will permit us to identify the

processes and constrain the microphysical parameters (e.g., sputtering yields) controlling the supply of lunar gas and its interaction with the surface.

2. Exospheric Abundances of Species Derived From the Lunar Surface

2.1. Model of Particle Transport

[8] The production and distribution of lunar exospheric constituents is modeled with an analytical model of particle transport in a collision-free exosphere [*Hartle*, 1971]. The model, which is a generalization of the *Chamberlain* [1963] model for nonuniform "exobase" density and temperature, uses Liouville's theorem to compute the normalized density of neutrals,

$$n(\mathbf{r}) = \int f(\mathbf{r}, \mathbf{v}) d\mathbf{v}, \tag{1}$$

given a truncated distribution function defined as:

$$f(\mathbf{r}, \mathbf{v}) = f_0(\mathbf{r_0}, \mathbf{v_0}) \times U(v_{r_0} > 0) \times \{1 - U(v_r < 0) \times U(v > v_{ESC})\}. \tag{2}$$

In this equation, the velocity vector, **v**, at a point, **r**, in the exosphere is related to the point ($\mathbf{r_0}$, $\mathbf{v_0}$) of the surface where it originates using the constants of motion under gravitational forces. f_0 ($\mathbf{r_0}$, $\mathbf{v_0}$) is the velocity distribution function of released particles from the surface. Finally, U is a unit step function that delineates the populated region of phase space, i.e., the integration limits: (1) particles must originate from the surface with outward radial velocities, $v_{r0} > 0$, and (2) particles may not return ($v_r < 0$) if they exceed escape velocity, v_{ESC}. It follows from equation (1) that the density anywhere in the exosphere can be computed with f of equation (2) provided that f_0 is known (section 2.1.1), and provided that the flux, $n_0 \langle v_{r\,0} \rangle$, is set to the surface source rate (section 2.3).

2.1.1. Sources

[9] As explained in the introductory comments, micrometeoroid impact vaporization and sputtering by solar wind ions are assumed to eject energetic atoms from the lunar surface. Additionally, UV photons acting upon the top monolayer of the surface can produce lower energy, but nonthermal, Na and K atoms. The atoms originate with initial speeds and directions that are characteristic of the source process, information that is captured in the assumed form of the distribution function of released atoms, f_0.

[10] 1. For impact vaporization, we assume a spatially uniform source of micrometeoroids that eject atoms with a Maxwellian distribution of upward velocities from the surface:

$$f_0 = (m/2\pi K_B T_0)^{3/2} e^{\frac{-m}{2K_B T_0} v_0^2}, \tag{3}$$

where v_0 the ejection speed, m is the mass of a considered atom, K_B is the Boltzmann constant, and $T_0 \sim 3000$–5000 K a "temperature" for ejecta from this process.

[11] 2. For photon-stimulated desorption (PSD), we assume that the ejected atoms (Na and K) originate from the dayside, and have a Maxwellian velocity distribution with $T_0 \sim 1200$ K and a dependence on solar zenith angle, χ_0, as:

$$f_0 = (m/2\pi K_B T_0)^{3/2} \cos\chi_0 e^{\frac{-m}{2K_B T_0} v_0^2}. \tag{4}$$

[12] 3. For sputtering, the energy distribution and directionality of the ejecta are described by a modified Sigmund-Thompson function:

$$f_0 = \frac{6E_b}{3 - 8\sqrt{E_b/E_{Max}}} \frac{E_0}{(E_0 + E_b)^3} \left\{1 - \sqrt{(E_0 + E_b)/E_{Max}}\right\} \cos\,\delta_0, \tag{5}$$

where E_0 is the ejected energy, E_b the binding energy of an atom to the surficial grain (e.g., $E_b = 2$ eV for sodium) and E_{Max} the maximum energy that can be imparted to the ejected surficial atoms. For the species studied here E_{Max} is typically a few hundred eV given the incidence onto the Moon of 1 keV solar wind protons, but such high ejection velocities are very improbable since $f_0 \approx E_0^{-2}$ at high energies. Due to the effects of soil porosity, the atoms are sputtered primarily perpendicular to the surface, with the yield assumed to reduce as the cosine of the angle, δ_0, with respect to the local vertical direction.

2.1.2. Sinks

[13] In our model only single hops are tracked, which assumes that atoms returning to the surface are adsorbed, or stick, with unit efficiency and are not rereleased. Losses to photoionization, computed from cross sections given in the work of *Verner et al.* (1996), are insignificant on timescales of a single ballistic trajectory except for Al atoms, which have the shortest ionization lifetime (~25 min). With this exception, the primary loss mechanisms in this model are ballistic escape and recycling to the surface. Although refractories and K are expected to stick upon striking the surface, this is a poor assumption for Na for which a few hops are likely to occur prior to sticking. This is because its measured sticking coefficient onto SiO_2 exhibits a strong temperature-dependence [*Yakshinskiy and Madey*, 2005]. Any partially thermalized sodium population due to energy exchange with the surface is excluded from our model because mainly high-altitude (≥100 km) observations of the dayside were used for its validation [*Sarantos et al.*, 2010].

[14] Other possible losses, most notably those relating to formation of molecular fragments and condensates, are neglected. Although relevant experiments are lacking, quenching theory predicts that gas condensation to solid grains in hypervelocity impacts may be an important loss process for impact-driven refractories [*Berezhnoy and Klumov*, 2008; *Berezhnoy*, 2010]. For Ca we find clear evidence of losses that are not included in the model (section 2.4).

2.2. Assumed Surface Composition

[15] Compositional estimates of the lunar surface are needed to initialize the model. Samples from four different types of soils have been brought back from the Moon: Highland, KREEP, low-Ti and high-Ti Mare soils [*Wurz et al.*, 2007; *Papike et al.*, 1982; *Heiken et al.*, 1991]. In

Table 1. Assumed Composition of the Lunar Regolith and Variation Across Soil Types[a]

Element	Low-Ti Mare Soils	High-Ti Mare Soils	Highland Soils	KREEP Soils
O	60.26	60.30	60.82	60.47
Si	17.30	15.86	16.31	17.35
Al	5.56	5.70	10.66	6.48
Mg	5.53	5.70	3.84	5.39
Ca	4.44	4.60	5.92	4.43
Fe	5.85	5.29	1.90	4.47
Ti	0.66	2.01	0.17	0.62
Na	0.26	0.31	0.29	0.44
K	0.06	0.05	0.05	0.19
Mn	0.08	0.07	0.03	0.06

[a]The lunar regolith composition assumed for these simulations is that of Low-Ti Mare soils, and the variation across soil types is the percent of relative abundance by number. Averages taken from *Wurz et al.* [2007]; original data from *Papike et al.* [1982].

broad terms, the elemental compositions of KREEP and Mare soils are similar, whereas highlands have more Al and less Fe, Mg and Ti. The largest elemental variations across soil types are found for Ti (factor of 10 more abundant in high-Ti Maria than in highlands), Fe (two to three times less abundant in highlands), and K (three times more abundant in KREEP soils). These differences, summarized in Table 1, introduce the first of many uncertainties in our model estimates. For the estimates provided throughout this paper we assume a low-Ti Mare soil composition.

2.3. Estimated Source Rates

[16] The vapor production rate by micrometeoroid impacts, which is a continuous source, was estimated using the model presented in the work of *Morgan and Killen* [1997] and its subsequent improvements [*Morgan and Killen*, 1998; *Killen et al.*, 2005]. A brief summary of how we simulate the physics of vaporization is given in the Appendix of this paper. The density of meteoroid material near Earth, an input parameter to the model, is assumed to be 3×10^{-16} g cm^{-3} for particles smaller than 1 cm [*Love and Brownlee*, 1993]. Two other parameters of the model determine the amount of vapor produced: the material types of the target and impactor. We have assumed that the impact parameters of aluminum onto enstatite and the regolith porosity of 0.5 can describe the interaction of stony-rich meteoroids with the lunar soil. Requiring impactors with speeds that exceed 5 km/s to vaporize refractories, the total vaporization rate for all species at R = 1 AU is $M_{vap} = 1.78 \times 10^{-16}$ g cm^{-2} s^{-1} from our code. The vapor cloud was assumed to be stoichiometric, $S_{IV} = c\ M_{vap}\ N_A$/(atomic weight), where S_{IV} is the production rate per species due to impact vaporization, c an elemental abundance in the soil, and N_A is Avogadro's constant. Given a low-Ti Mare composition, impacts produce an estimated 4×10^6 O atoms cm^{-2} s^{-1}, while for a species like Mg we obtain 2.5×10^5 atoms cm^{-2} s^{-1}. The assumed temperature for this source process is $T \approx$ 3000–5000 K, close to the experimental values for hypervelocity impacts [e.g., *Eichhorn*, 1978]. We have not estimated the fraction of a given species that may be ejected in molecular form. Nor do we consider the possibility that some of the products may be ionized in the vapor plume.

[17] The production rate due to PSD may be estimated by assuming a sodium surface density $\sigma \sim 3 \times 10^{12}$ cm^{-2}, a flux $F_{ph} \sim 2 \times 10^{14}$ cm^{-2} s^{-1} of UV photons (≥5 eV) and an effective PSD cross section $Q \sim 3 \times 10^{-21}$ cm^2 [*Yakshinskiy and Madey*, 1999]. This results in a source rate, $\sigma \times Q \times F_{ph}$, of 2×10^6 atoms cm^{-2} s^{-1} at the subsolar point. This model setup was found to agree within a factor of 2 with the sodium ground-based observations [*Sarantos et al.*, 2010]. For potassium we assumed the same effective PSD yield as sodium. The effective temperature inferred from the laboratory experiments is $T \approx$ 1200 K for this process.

[18] The production rate due to ion sputtering was obtained by the following assumptions: a sputtering yield $Y = 0.05$ per ion impact [e.g., *Wurz et al.*, 2007]; a typical precipitating flux $F_{SW} = 4 \times 10^8$ solar wind ions cm^{-2} s^{-1}; and the elemental number abundance, c, of a species of interest in the regolith (Table 1). These parameters yield a sputtered flux per species, $S_{SPUTT} = cY F_{SW}$, that amounts to 1.2×10^7 O atoms cm^{-2} s^{-1} (1×10^6 Mg atoms cm^{-2} s^{-1}) at the subsolar point. At other solar zenith angles, χ_0, this flux was assumed to decrease as $\cos\chi_0$ due to the increased angle of solar wind incidence. A small ∼4° difference between the solar zenith and solar wind incidence angle that is due to aberration was neglected.

2.4. Model Results and Comparisons With Existing Measurements

[19] Model simulations of the expected release processes for several species are shown in Figures 1 and 2. All processes reflect the composition of the lunar surface, but the rates and velocity distributions are different, meaning that atoms from each source are distributed differently near and far from the surface. Within uncertainties in the micrometeoroid influx and the sputtering yield, which are discussed at length in section 2.5, impact vaporization and ion sputtering are found to contribute approximately equally to the release of gas over the subsolar region for fluxes typical of the solar wind at 1 AU. For exospheric refractories the two sources can be separately constrained in the vicinity of the Earth's magnetosphere by measuring the relative increase in exospheric levels when the Moon is exposed to the solar wind. Photon-stimulated desorption of Na and K greatly exceeds release of these two species by impacts and sputtering as previously surmised [e.g., *Sarantos et al.*, 2010]. Estimated number densities at LADEE altitudes from this model, shown in Figure 2, are small and generally less than the ∼100 atoms cm^{-3} predicted for O by the combined action of impacts and the solar wind. The gas densities could be even lower if formation of stable molecules and/or solids occurs.

[20] Zenith (vertical) column abundances from the model are compiled in Table 2, along with available upper limits from the Moon. Those limits, obtained from lines of sight tangential to the surface, were converted to zenith column densities using a *Chamberlain* [1963] model of uniform ejection at T = 400 K [*Stern*, 1999]. The least stringent upper limit is that for lunar Mg because Hubble Space Telescope (HST) bright object avoidance constraints did not permit tangent heights any closer than 2000 km from the surface [*Stern et al.*, 1997].

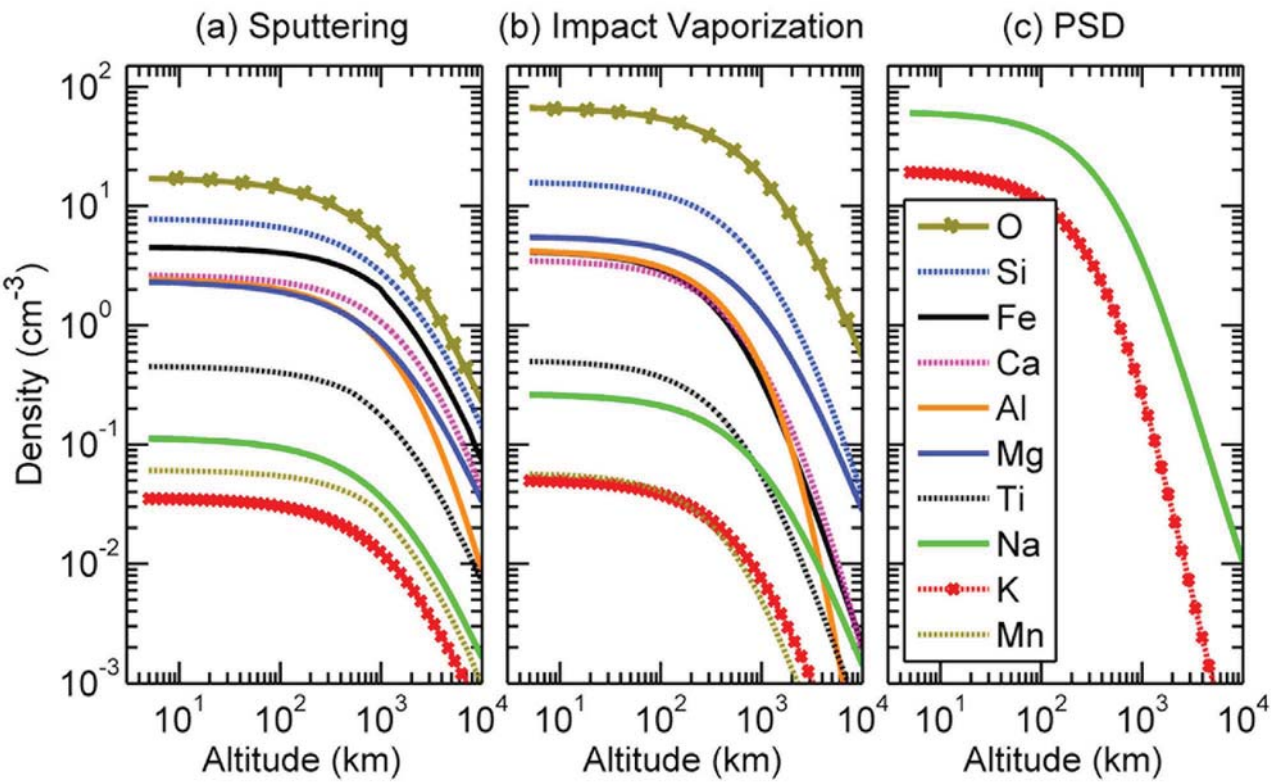

Figure 1. Model predictions of lunar exospheric refractories over the subsolar point.

[21] The model predicted ratio of Na/K in the exosphere is four to five at low altitudes, in agreement with the 6 ± 3 Na/K abundance ratio obtained from observations [*Potter and Morgan*, 1988]. The modeled column abundances for Fe and Mg are below the upper limits quoted in Table 2, while those for Al and O approach their upper limits. Modeled Si and Ti are four to six times above the upper limits, but these limits were derived from transitions between extremely excited states (section 4.1). Only Ca is found to be unquestionably overestimated by our model. The deficiency

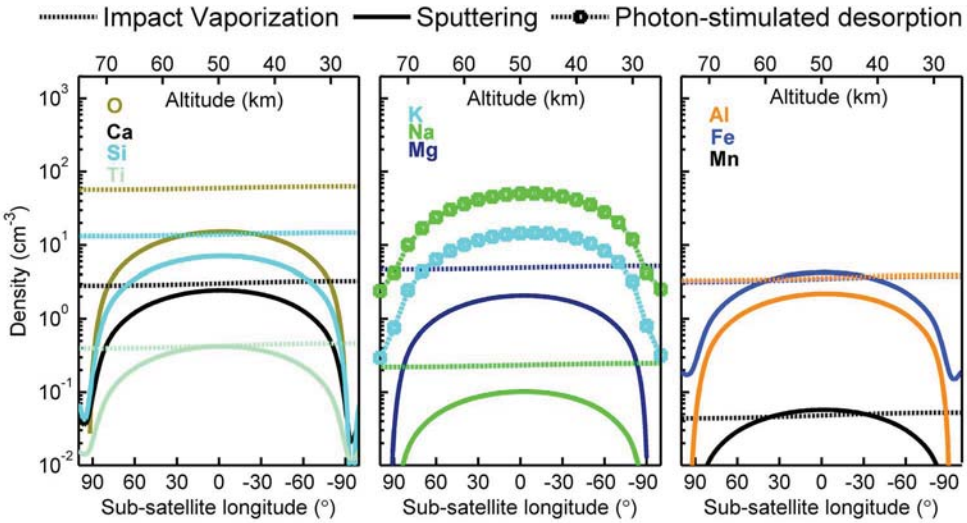

Figure 2. Exospheric densities that would be encountered by LADEE along an equatorial orbit (25 × 75 km) from impact vaporization (denoted by nearly horizontal dotted lines), sputtering, and photon-stimulated desorption (for Na and K). The spacecraft location is indicated by both a sub-satellite longitude (where dawn = −90° and dusk = +90°) and by an altitude above the surface (where dawn = 25 km and dusk = 75 km).

Table 2. Modeled Zenith Column Abundances Compared to Known Upper Limits at the Moon[a]

	Impact Vapor Model		Sputtering Model		PSD Model		Detections[b] or Upper Limits[c]	
	n_0 (cm^{-3})	Zen.Col. Abundance (cm^{-2})	Subsolar n_0 (cm^{-3})	Subsolar Zen.Col. Abundance (cm^{-2})	Subsolar n_0 (cm^{-3})	Subsolar Zen.Col. Abundance (cm^{-2})	n_0 (cm^{-3})	Zen.Col. Abundance (cm^{-2})
Na	0.3	2.2E07	0.1	1.4E07	60	1.9E09	67 ± 12	8 ± 3E08
K	0.05	2.9E06	0.03	4.7E06	19	3.5E08	15 ± 3	1.4 ± 0.3E08
Mg	5.5	4.5E08	2.3	2.8E08	—	—	≤6000	≤5.4E10
Ca	3.5	1.7E08	2.6	3.9E08	—	—	≤1	≤5.0E06
Al	4.2	1.8E08	2.4	2.3E08	—	—	≤55	≤4.3E08
Fe	4.1	1.6E08	4.5	7.1E08	—	—	≤380	≤1.3E09
Ti	0.5	2.3E07	0.5	6.6E07	—	—	≤1	≤4.0E06
Si	15.6	1.1E09	7.7	1.1E09	—	—	≤48	≤3.6E08
O	66.3	6.2E09	16.9	1.9E09	—	—	≤500	≤7.4E09

[a]Modeled column abundances were computed out to 1 Hill sphere for the Moon, approximately 35 lunar radii.
[b]Lunar Na and K abundances are from the discovery measurements of *Potter and Morgan* [1988].
[c]Limiting Zenith column abundances for unobserved species are Chamberlain fits of limiting tangential column abundances assuming T = 400 K [*Stern*, 1999].

of measured Ca most likely implies losses to condensation and molecular formation that are not included in the model [*Berezhnoy and Klumov*, 2008; *Berezhnoy*, 2010]. Notably, the predicted Ca sputtered component alone exceeds the observed upper limits. The mean solar wind flux on the day of that observation, 30 July 1994 [*Flynn and Stern*, 1996], was 2.65×10^8 protons cm^{-2} s^{-1}, about half of what we assume in our baseline model, and the Moon was at quarter phase, clearly exposed to the solar wind. At these flux levels, the sputtered model would be consistent with the measurement if we assumed a sputtering yield of no more than 0.01 ions/s.

[22] In conclusion, clear deviations from a stoichiometric model (impacts plus sputtering) is seen only in the case of Ca, which may be ejected in molecular form. For other undetected species, including oxygen, modeled abundances are either clearly below published limits, or do not differ significantly from measured limits given uncertainties in surface soil abundance, micrometeoritic influx, and sputtering yields. Without further measurements, we may only infer that the column abundance of refractories to Na and K can be explained by the effect of PSD, a process that is specific only to alkalis. Improved spectroscopic observations closer to the Moon, such as those planned by LADEE, are required to elucidate the production and loss of these undetected species of the lunar exosphere.

2.5. Model Uncertainties

[23] Estimates of impact–driven production rates differ by roughly a factor of 5 because of uncertainties in the physical properties of the regolith and the impactors, the assumed micrometeoroid mass flux and velocity, and the method used to calculate the vapor yields [e.g., *Cintala*, 1992; *Killen et al.*, 2005]. Another estimate of the steady state total vapor flux for all species at Earth's Moon is 8.46×10^{-17} g cm^{-2} s^{-1} compared to our rate, 1.78×10^{-16} g cm^{-2} s^{-1} [*Bruno et al.*, 2006]. Thus, our calculation agrees within a factor of 2 with other models. Our vapor predictions include the vapor produced by the volatilization of the impactors but do not account for the possible enhancements of impact vapor during encounters with meteoroid streams.

[24] The sputtering yields of neutrals are highly uncertain for numerous reasons. We have assumed here a common sputtering yield of $Y = 0.05$ atoms per incident ion for all species to establish a baseline model. This number is generally in agreement with the results of *Wurz et al.* [2007], who included the mineralogy and solar wind energy dependence in TRIM simulations. But solar wind ions can sputter both atoms and ions from lunar soils with an uncertain partitioning. When bombarded with solar wind–like 1–4 keV H^+ and He^+ ions, lunar soil simulants produced secondary lunar ions at fluxes of $\sim 10^3$–10^4 ions cm^{-2} s^{-1} per species [*Elphic et al.*, 1991]. The flux of secondary ions was found in that experiment to anticorrelate with the ionization potential such that elements with low ionization potential (K^+, Na^+, Ca^+, Al^+) had the highest ion yield. Fluxes of $\sim 10^3$–10^4 ions cm^{-2} s^{-1} are only ~1% of the neutral production rate assumed for a given species in our simulation. However, results from more recent experiments on sodium-bearing silicates appear to suggest that almost all sputtered Na leaves the surface as ions, not as neutrals [*Dukes et al.*, 2011]. The same experiment revealed that large fractions of other sputtered species, like Al and Si, are sputtered off as ions. Hence, it is possible that species with low ionization potential leave the surface ionized. If this hypothesis is correct, relatively smaller neutral sputtering yields should be expected for species such as K, Na, and Ca, and relatively higher sputtering yields may be expected for neutral O. Finally, it is unclear to what extent multiply charged solar wind ions enhance the yield from a planetary regolith although highly charged ions have been shown to enhance yields from idealized surfaces [*Aumayr and Winter*, 2004; *Meyer et al.*, 2011]. Note that LADEE will be observing at the Moon during solar maximum.

[25] The most significant uncertainties are losses to molecular formation and to the formation of solid grains (condensation) during impacts. Molecules can be produced in the vapor + liquid + solid phase that follows micrometeoroid impact [*Berezhnoy and Klumov*, 2008; *Berezhnoy*, 2010] and, followed by dissociation, they can produce high-energy atoms of Mg, Ca, O, as well as other species. Very energetic Mg and Ca atoms observed in Mercury's tail have been attributed to a dissociating molecular source [*Killen et al.*, 2005; *McClintock et al.*, 2009; *Killen et al.*, 2010]. We know neither the abundance ratio of atoms versus molecules of the same species in the vapor cloud, nor the molecular dissociation lifetime and temperature. Short molecular lifetimes (≤2 min) and ratios of molecules-to-

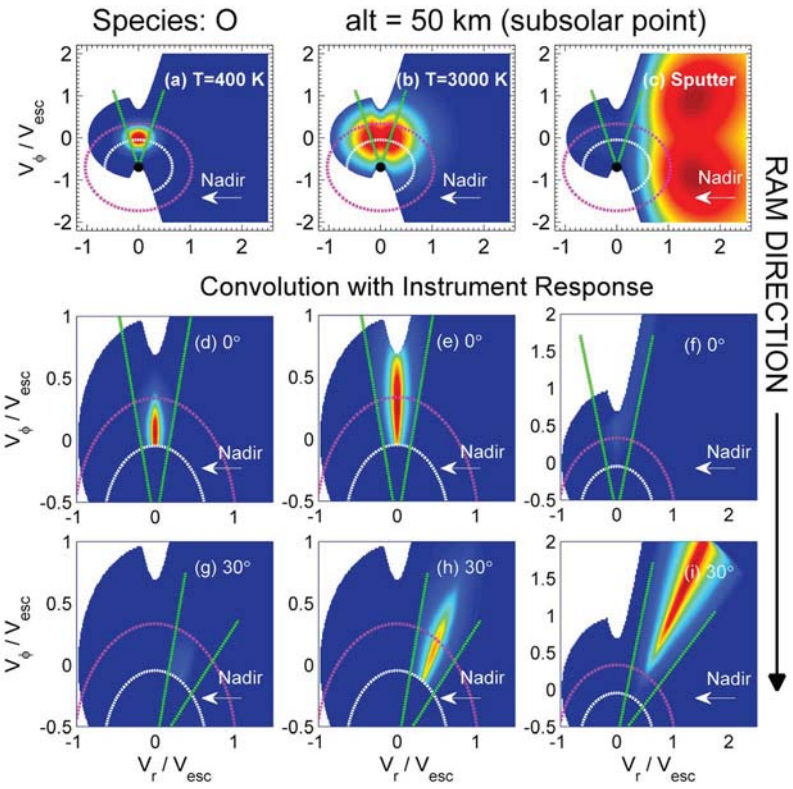

Figure 3. (top) Velocity distribution of lunar exospheric particles in the equatorial plane: (a) Oxygen accommodated to the local surface temperature; (b) oxygen from micrometeoroid impact vaporization; (c) oxygen from sputtering. (middle and bottom) Based on these three theorized velocity distributions, the relative fraction of neutrals that map into the open source LADEE NMS (black dot) is shown for ram (0°) and 30° off-ram pointings: (d) and (g) thermal processes; (e) and (h) impacts; (f) and (i) sputtering. Dotted green lines indicate the instrument's effective field of view. Dotted white (magenta) circles centered on the spacecraft indicate the fraction of planetary neutrals not measured when the instrument cut-off energy is 0.2 eV (0.5 eV).

atoms of ∼4:1 must be inferred from modeling of MESSENGER observations of Mg if fast atoms in the tail are produced by dissociating molecules [*Sarantos et al.*, 2011]. But an estimate of the gas-to-solid fraction cannot be made without measuring the dissociation rate of the putative molecules in the laboratory. If stable gas molecules form, the local density of atomic elements driven by impacts is lower than the best-case estimates because a fraction of the molecular population returns to the surface before it is dissociated. Refractories condense in the following degree: Al and Ti > Ca > Si > Mg and Fe. According to quenching theory, the fraction remaining in the gas phase is ≤1% for Al and ≤5% for Ca at T ≤4000 K. At even lower temperatures, T = 3000 K, Si < 1%, and Mg ∼ Fe ∼ 5% in the gas phase [*Berezhnoy*, 2010]. Na and K do not condense. Because of these possibilities (condensation plus molecular formation), the model abundances for refractory elements are probably upper limits as it was deduced from measured Ca.

3. Neutral Mass Spectroscopy

[26] The neutral mass spectrometer (NMS) onboard LADEE is based on a variation of the design of the Cassini Ion and Neutral Mass Spectrometer (INMS) [*Waite et al.*, 2004]. Although its primary goal is the detection of lunar volatiles, the instrument will search for the species studied in this paper using its open source. The NMS open source is designed specifically to measure wall-reactive species, one mass-to-charge ratio at a time, and has a relatively narrow field of view that excludes particles that map into the instrument with large entry angles relative to its optical axis [*Delory et al.*, 2009]. Due to the nature of the instrument design, the detection efficiency is also energy dependent. A description of this instrument and of its principal specifications can be found in the INMS calibration paper [*Waite et al.*, 2004].

3.1. Description of the NMS Measurements of Refractories

[27] To illustrate how the NMS open source samples exospheric gases, Figure 3 shows the populated portion of the velocity space in a Selenocentric system for Oxygen neutrals at the orbital altitude of 50 km above the subsolar point. We assume that these Oxygen atoms originate from the lunar surface with three hypothetical distributions: (1) a Maxwellian with a temperature of 400 K that describes

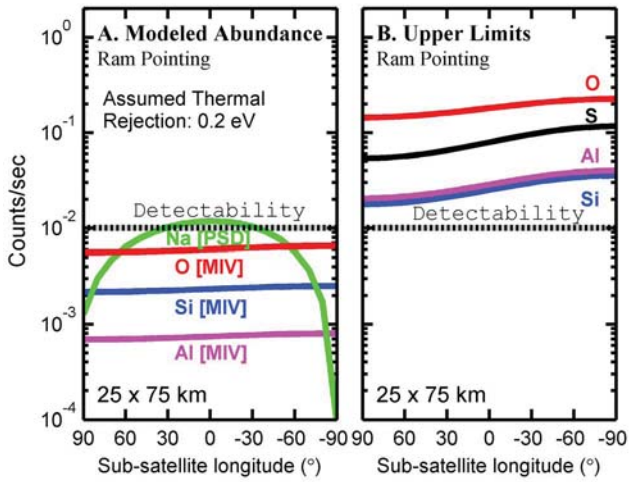

Figure 4. Estimated signal levels (c/s) were computed from the convolution of a LADEE NMS proxy response with (a) modeled three-dimensional distributions from micrometeoroid impact vaporization (MIV) and photon-stimulated desorption (PSD); and (b) modeled upper limits [*Stern*, 1999] which implicitly assume the accommodation of lunar exospheric particles to the surface temperature (T = 400 K). Models on the left and right are equivalent in terms of total *column abundance* (Table 2), yet they differ in estimated counts because for cooler sources the near-surface *number abundance* is higher. "Detectability" is taken to be the level of instrument noise. The calculations exclude particles which arrive into the instrument with $E \leq 0.2$ eV.

thermally accommodated ejecta, (2) a Maxwellian with a temperature of 3000 K that describes impact vaporization; and (3) a sputtering distribution.

[28] In Figure 3(top), the two-dimensional distribution of local velocities is shown as a function of radial velocity, v_r, and the projection of the tangential component onto the plane of the orbit, v_φ. (The distribution function shown has been integrated for the out-of-the plane component.) In the middle and bottom rows, the three-dimensional distribution function for each of these sources was convolved with a proxy instrument response for different boresights. The location of the spacecraft in this frame of reference is denoted by a black dot. The white space indicates the envelope of particle trajectories that connect to the surface, i.e., the limits of integration of equation (1). An instrument field of view of $\pm 20°$ is depicted by green dotted lines. Figure 3 relates specific aspects of NMS measurements of refractories:

[29] 1. For thermally accommodated neutrals (Figure 3a), the field of view of the open source encompasses a large fraction of the neutral distribution.

[30] 2. In contrast, for ejecta generated by impact vaporization and sputtering (Figures 3b and 3c), the open source field of view captures only a small portion of the particle phase space.

[31] 3. For speeds typical of a lunar orbiter the instrument overall sensitivity depends critically on its response to low-energy particles. The dotted white circle around the spacecraft is the locus of neutral particles that arrive at the instrument with energies ≤0.2 eV; the dotted magenta circle encloses particles with energies ≤0.5 eV (in the instrument's reference frame). It is clear that in order for the mass spectrometer to detect exospheric particles from a T ≤ 3000 K source, the instrument energy cut-off should be lower than 0.5 eV.

[32] 4. The sensitivity is a function of pointing direction and temperature. For near–Maxwellian sources pointing toward ram is preferable. For directional, high-energy sources, such as sputtering, very few particles arrive at the spacecraft with near-zero radial velocity. Therefore, pointings larger than ~30° from ram (toward nadir) would provide the best chance for detecting sputtered particles.

3.2. Model Convolution for Refractory Species With the LADEE NMS Response

[33] In Figure 4 a simplified proxy of the NMS open source response is convolved with the three-dimensional velocity distribution function for a number of exospheric refractories to derive the expected signal levels (counts per second) for ram pointing as a function of spacecraft location and source temperature. Based on preliminary instrument calibration results, we assume a nominal sensitivity of 10^{-2} (counts/s) per (particle/cc), an energy cut-off of 0.2 eV (particles with energies lower than 0.2 eV will not be detected), and a detector noise level of 0.01 counts/s. Note that the instrument sensitivity for some species will be better than assumed here due to their increased electron impact ionization cross sections.

[34] Assuming high-energy velocity distributions (Figure 4, left), our calculations indicate that modeled O, Si (impacts) and Na (PSD) should correspond to signal levels that are near instrument noise levels, whereas other metallic species are undetectable. The maximum instrument signal levels were estimated in Figure 4(right) using the upper limits given in the work of *Stern* [1999] with T = 400 K (low-energy distributions). In that case, all species but Ti are detectable due to the higher local density and the greater fraction of phase space that NMS observes for low-temperature sources. Note that models on the left and right are effectively equivalent in terms of column abundance (Table 2). Models on the left are "preferable" because an energetic parent process is required to vaporize refractories.

Table 3. Fraction of Phase Space Seen by the Open Source LADEE NMS as a Function of Assumed Source Temperature[a]

Element	Fraction Observed (%)	Density (cm^{-3}) Corresponding to S/N = 2	Density (cm^{-3}) at Periapse alt = 25 km
Hot O (3000 K)	1.0	200	63
Cold O (400 K)	5.5	36	412
Hot Si (3000 K)	1.6	125	15
Cold Si (400 K)	10.0	20	34
Hot Na (1200 K)	2.4	83	50
Sputtered O	0.2	1000	14

[a]The density corresponding to S/N = 2 was calculated assuming NMS. Sensitivity = 0.01 (cts/s)/(atoms/cm^3) and Noise = 0.01 cts/s; no transmission of neutrals entering the instrument with E ≤ 0.2 eV is assumed; Na is shown over the subsolar point (altitude = 50 km); Sputtering computed for pointing = 30° toward nadir; Else, ram pointing is shown; "Cold" Si, and O are computed from upper limits [*Stern*, 1999]; "Hot" Si and O are computed from impact vaporization model; "Hot" Na from PSD model.

Table 4. Strongest Emission Lines of Regolith-Derived Exospheric Species in the LADEE UVS Range[a]

Species	Wavelength Vac (Å)	Wavelength Air (Å)	Ei (cm^{-1})	*g_value*
Fe I	2523.608	2522.849	0	4.0E-03
Fe I	2719.833	2719.027	0	7.7E-03
Fe I	3720.99	3719.935	0	6.76E-03
Fe I	3859	3859.91	0	4.57E-03
Al I	3083.048	3082.1529	0	4.87E-03
Al I	3093.6078	3092.7099	112.061	4.68E-03
Al I	3945.1222	3844.0058	0	1.83E-02
Al I	3962.641	3961.520	112.061	3.64E-02
Si I	2507.66	2506.90	77.115	1.66E-03
Si I	2515.08	2514.32	0	2.1E-03
Si I	2516.87	2516.11	223.157	2.4E-03
Si I	2519.96	2519.2	77.115	1.58E-03
Si I	2524.87	2524.1	77.115	1.34E-03
Si I	2529.27	2528.5	223.157	2.60E-03
Ti I	3187.37	3186.451	0	2.95E-02
Ti I	3192.92	3191.99	170.132	2.10E-02
Ti I	3342.84	3341.88	0	2.06E-02
Ti I	3371.41	3370.44	0	2.2 E-02
Ti I	3636.50	3635.46	0	8.73E-02
Ti I	3643.72	3642.68	170.13	5.61 E-02
Ti I	3948.90	3947.77	170.13	5.62E-02
Ti I	3949.79	3948.67	0	5.62E-02
Ti I	3957.46	3956.34	170.13	4.1E-02
Ti I	3959.33	3958.21	386.87	6.0E-02
Ti I	3982.89	3981.76	0	6.78E-02
Ti I	3983.61	3982.48	0	1.80E-02
Ti I	3990.89	3989.76	170.13	6.92E-02
Ti I	3999.77	3998.64	386.87	6.87E-02
Mg I	2852.96	2852.127	0	3.2E-02
Ca I	4226.73	4227.92	0	4.9E-01
Na I	3303.32	3302.37	0	5.41E-04
Na I	3303.93	3302.97	0	5.85E-04
Na I	5891.6	5889.95	0	5.25E-01
Na I	5897.6	5895.92	0	3.07E-01
K I	4045.2	4044.136	0	3.1E-02
K I	4048.4	4047.28	0	1.26E-02
KI	7667.01	7664.89	0	2.76E0
K I	7701.08	7698.96	0	1.94E0
Mn I	2795.64	2794.82	0	2.8E-02
Mn I	2799.09	2798.27	0	2.17E-02
Mn I	2801.89	2801.06	0	1.5E-02
Mn I	4031.90	4030.76	0	1.5E-02
Mn I	4034.21	4033.07	0	1.09E-2
Mn I	4035.63	4034.49	0	7.64E-03

[a]Listed are *g* values at zero Doppler shift. The range is 2316–8259 Å.

[35] Should two populations be present, we quantify in Table 3 the fraction of local density seen by the instrument as a function of species mass and temperature, and estimate the minimum density that results in a signal-to-noise ratio of two. This was given assuming an optimal pointing direction (30° toward nadir for sputtered species, and ram pointing for the rest). LADEE NMS can detect O to a limit of ~36 atoms cm^{-3} with its open source, which is less than the estimated density of cold O at 25 km; therefore LADEE can answer the question of whether oxygen is hot or not. No sputtered species can be detected at the assumed levels of instrument sensitivity because the very small fraction of phase space seen, 0.2–0.3%, necessitates sputtered densities exceeding 1000 atoms cm^{-3} for a reasonable signal-to-noise ratio (SNR). These results are obviously dependent on the assumed instrument cut-off energies and noise levels and should be revised as the performance of the actual mass spectrometer is measured during calibration.

[36] For completeness, we provide estimates for sulfur, a species of meteoritic origin that should be accessible for detection using the mass spectrometer's open source. If an upper limit of 150 S atoms cm^{-3} at the surface and a temperature of 400 K are assumed [*Stern*, 1999], we predict ~1 c/ 10 s at a periapse of 25 km, which should be detectable by NMS.

4. Ultraviolet-Visible Spectroscopy

4.1. Main Emission Lines and *g* Values in the UVS Spectral Range (230–825 nm)

[37] We obtained the *g* values for the primary Na, K, Mg, and Ca lines that were recently calculated for Mercury [*Killen et al.*, 2009] and scaled them to 1 AU for the Moon. For other species of interest we calculated improved resonance scattering *g* values (Table 4) that include the effects of fluorescence [*Chamberlain and Hunten*, 1987, equation (6.2.4)]. High-resolution solar flux spectra were obtained from *Kurucz et al*. [1984], whereas the oscillator strengths were obtained from the NIST database [*Ralchenko et al.*, 2010]. Some of these *g* values are plotted in Figure 5 as a function of an atom's radial velocity with respect to the Sun. The lines for each species we chose to list in Table 4 are the ones having the strongest *g* values. This means they are generally ground state transitions. We find that some of the most prominent emission lines of undetected species in the UVS spectral range, ~200 – 800 nm, are: Si (2515 Å, 2517 Å, 2529 Å); Fe (2719 Å, 3720 Å); Al (3944 Å, 3962 Å); and Ti (e.g., 3636 Å, 3983 Å, 3991 Å, 3999 Å, and many more). The relative ease of detection of a line is also a function of instrument sensitivity, which is wavelength dependent and decreases at smaller wavelengths, but not markedly (see next section).

[38] The following findings must be noted:

[39] 1. The *g* value for Al (3092 Å) is an order of magnitude less than the *Morgan and Killen* [1997] value. There is a deep solar Fraunhofer line nearby and a high-resolution solar spectrum may not have been available at the time.

[40] 2. The effect of fluorescence (pumping from other levels) is significant for Si (2515 Å, 2519 Å, 2529 Å) and Al (3944 Å, 3962 Å) lines. Due to this effect the Al emission at 3962 Å is twice that of Al at 3944 Å.

[41] 3. The Al and Ti *g* values show a strong dependence on radial velocity. This result means that sputtered Al and Ti atoms (highly directional toward the Sun on the dayside) see a much larger portion of the solar continuum and will scatter light much more efficiently than impact-driven atoms from these species. This effect was not included in our baseline simulations (sections 4.2 and 4.3), which all assumed a *g* value at zero Doppler shift.

[42] 4. Oscillator strengths relating to transition probabilities for Al I lines of Table 4 are given an 18–25% accuracy in the NIST tables. The oscillator strengths for Si and Ti are known to 10–25% accuracy.

[43] 5. The Si I line at 3906 Å, on which the upper limit reported for Si by *Flynn and Stern* [1996] was based, originates from a level 5 eV to a level 6.9 eV above the ground state. The lower level is not expected to be highly populated, thus this is not a resonance transition. Likewise, the Ti I 5036 Å line, monitored by *Flynn and Stern* [1996],

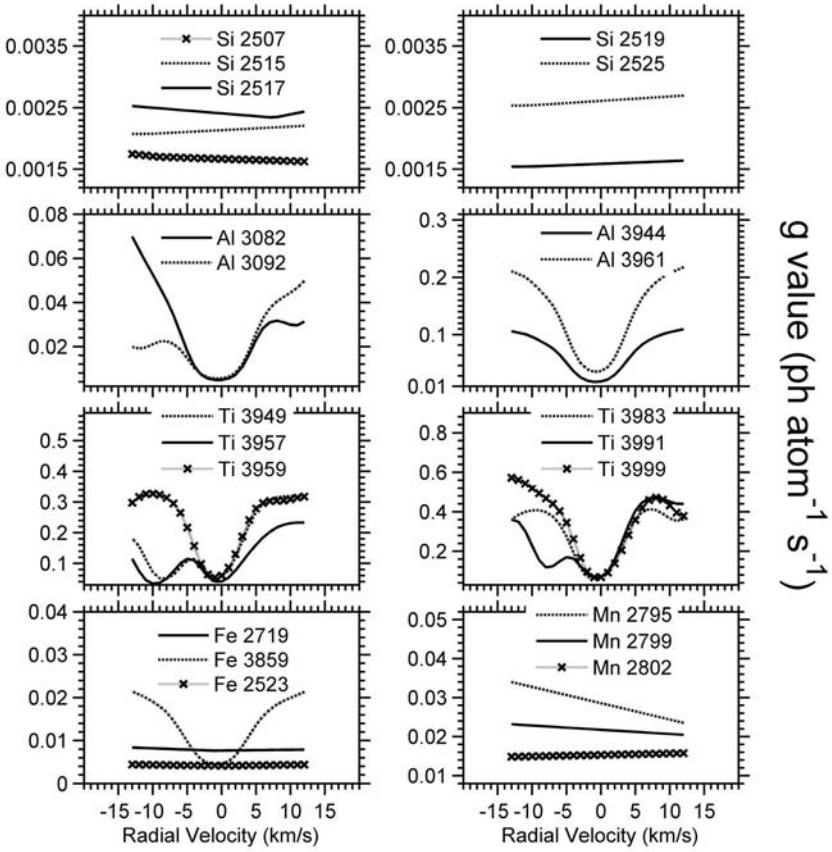

Figure 5. The *g* values at r = 1 AU are shown as a function of an atom's velocity (with respect to the Sun) for the main lines of regolith-derived constituents of the lunar exosphere. For Mg, Ca, K, and Na lines see *Killen et al.* [2009].

originates from a highly excited state, and thus unlikely to be populated.

[44] Assuming thermodynamical equilibrium and correcting for the probability of these excited states to be populated at T = 3000 K (e.g., from an impact vapor source), we estimated the *g* value for Si (3906 Å) to be 7.9×10^{-5} and that for Ti (5036 Å) to be 7.53×10^{-3}. To estimate upper limits for Si and Ti from measurements, *Flynn and Stern* [1996] assumed the *g* value for Si (3906 Å) to be 5.8×10^{-2} and that for Ti (5036 Å) to be 6.8×10^{-1}. These findings suggest that there are significant uncertainties associated with the published upper limits for Ti and Si. Our models of Si and Ti production suggest that column abundances a few times higher than those inferred by *Flynn and Stern* [1996] can be expected for these species.

4.2. Modeled Line Emission

[45] Given these *g* values, we computed intensities of the strong emission lines from nine species of interest within the range of UVS spectral coverage (230–825 nm). Sightlines for these simulations lie in the equatorial plane and have low-altitude tangent heights (10–40 km). Figure 6 shows the known species, Na and K, due to a PSD source. With anticipated emission of a few kiloRayleighs in their main lines, the spatial distribution of Na and K can be clearly observed on the dayside. Hence, the LADEE measurements, in tandem with models, will constrain not only the source rates for these species, but also the energy exchange of exospheric particles with the surface: the sticking and the thermal accommodation coefficients.

[46] Emission estimates from undetected species at levels expected from impact vaporization and sputtering

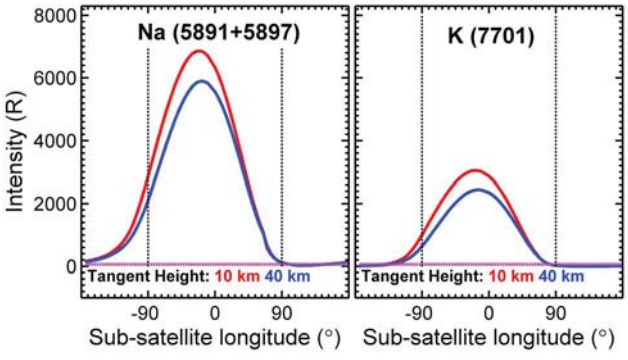

Figure 6. Modeled intensity for Na and K from a PSD source for equatorial lines of sight pointing from the spacecraft to the constant tangent altitude of 10 (red) and 40 km (blue).

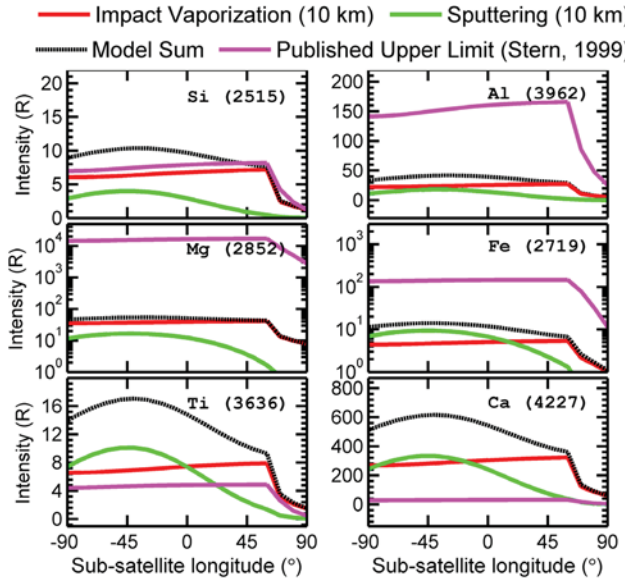

Figure 7. The modeled intensity from impact vaporization (red) and sputtering (green) for Si, Al, Mg, Fe, Ti, and Ca is compared to published upper limits [*Stern*, 1999].

are shown in Figure 7. Assumptions for impact vaporization are stated in section 2.3, i.e., total impact vapor rate of 1.78×10^{-16} g cm^{-2} s^{-1}, T = 3000 K, and no condensates or molecules for a "best case" estimate. For sputtering, the common sputter yield of 0.05 atom/ion and the solar wind flux of 4×10^8 ions cm^{-2} s^{-1} were assumed. We also show in Figure 7 the intensity that is consistent with the published limits from *Stern* [1999] using the Chamberlain model of T = 400 K. Our simulations predict that, at stoichiometric levels, emission in the range of 10–50 R may be expected with this geometry from many of the species studied here. The line intensity predictions shown in Figure 7 and the anticipated spectral performance of the UVS were used to simulate limb measurements by LADEE (section 4.3). For Ca we used the published upper limits because the modeled abundances were too high. In our simulations of UVS measurements we included modeled lines for Mn, which are not shown in Figure 7.

4.3. UVS Spectral Simulations

[47] The UVS instrument is a modified Czerny-Turner spectrometer and is nearly identical in design to the Visible Spectrometer (VSP) on the Lunar Crater Observation and Sensing Satellite (LCROSS) experiment [*Ennico et al.*, 2012]. It functions as a fiber-coupled "point" spectrometer with approximately 1° field-of-view, and it images all wavelengths onto a CCD array simultaneously, enabling the detection of trace elements. Measurements of lamp emission lines during VSP ground calibration showed that spectral resolution ($\lambda/\Delta\lambda$) decreased with wavelength, with average values for $\Delta\lambda$ of 0.66, 0.98 and 1.03 nm at wavelengths of 500–600, 400–500 and 300–400 nm, respectively [*Ennico et al.*, 2010, 2012].

[48] To create each UVS simulation, monochromatic line radiances were smoothed by convolving with a Gaussian passband function using a wavelength-dependent width that conforms to the VSP measurements. This was accomplished by performing the convolution using a deformed wavelength coordinate (λ') in which $\Delta\lambda'$ is constant, and then remapping the result back into the original set of wavelength points [*Georgiev et al.*, 2002]. The blurred spectra were then resampled at 0.56 nm point spacing which matches the sampling during tests of the UVS Engineering and Test Unit (ETU). Finally, Gaussian noise was added at the levels anticipated for this instrument. The sensitivity of the UVS ETU has been measured using calibrated incandescent and UV lamp sources (A. Colaprete, personal communication, 2011). Values of noise equivalent radiance (NER) between 40 and 45 Rayleigh nm^{-1} were measured between ~400 and 580 nm (we define NER as the radiance of a source that would produce a signal-to-noise ratio of unity in a 1 s integration time). Minimum detectable radiance increases slowly in the UV to ~70 R nm^{-1} at 250 nm, although the UV source calibration loses accuracy shortward of ~300 nm. It likewise increases to a value of ~150 near the long wavelength limit of UVS coverage (830 nm). Simulations for longer integration times were created by coaddition, assuming that the noise follows a Poisson statistical law.

[49] Line detection simulations are presented in Figure 8 as a function of spacecraft location, assuming a constant tangent height of 10 km and 60 s integration. Each simulation also shows the line spectrum (shifted downward by 80 R nm^{-1} for clarity) as it would be observed without instrument noise.

[50] As LADEE approaches orbital sunset, coronal-zodiacal light (CZL) becomes a significant excess brightness component, because the UVS line-of-sight is aft pointing and lies within a few degrees of the Sun. The brightness of CZL at UV-Vis wavelengths close to the Sun has been quantitatively mapped from lunar orbit during Apollo 16 coronal photographic sequences [*Macqueen et al.* 1973] and later using calibrated measurements by the Clementine Star Tracker cameras [*Hahn et al.*, 2002]. Along the ecliptic equator, brightness diminishes with increasing solar elongation angle (ε) as

$$CZL = Const\ \varepsilon^{-2.45\pm0.05} \quad (6)$$

a result that is valid between ~3° to at least 30° in ε [*Hahn et al.*, 2002]. The color of CZL is known from rocket-borne photometry [*Pitz et al.*, 1979] and photometric measurements made by the Helios spacecraft (see review by *Leinert et al.* [1998]) and is mildly reddened relative to solar irradiance. Combining equation (6) with the known spectral response of the Clementine Star Tracker camera [*Hahn et al.*, 2002] and CZL photometry, one can model [c.f. *Stubbs et al.*, 2010] the spectral radiance of CZL as seen by the UVS. This is shown in the bottom two panels of Figure 8, where the solar elongation angle along the line-of-sight is 22° and 12°, respectively. The CZL contribution by itself with instrument noise omitted is shown shifted upward by 80 R nm^{-1}. Zodiacal light is not an intrinsic noise source, since it can be modeled and (if needed) removed from the measurements, typically to a level smaller than the instrument noise. The comparisons shown in Figure 8 demonstrate that CZL strongly influences

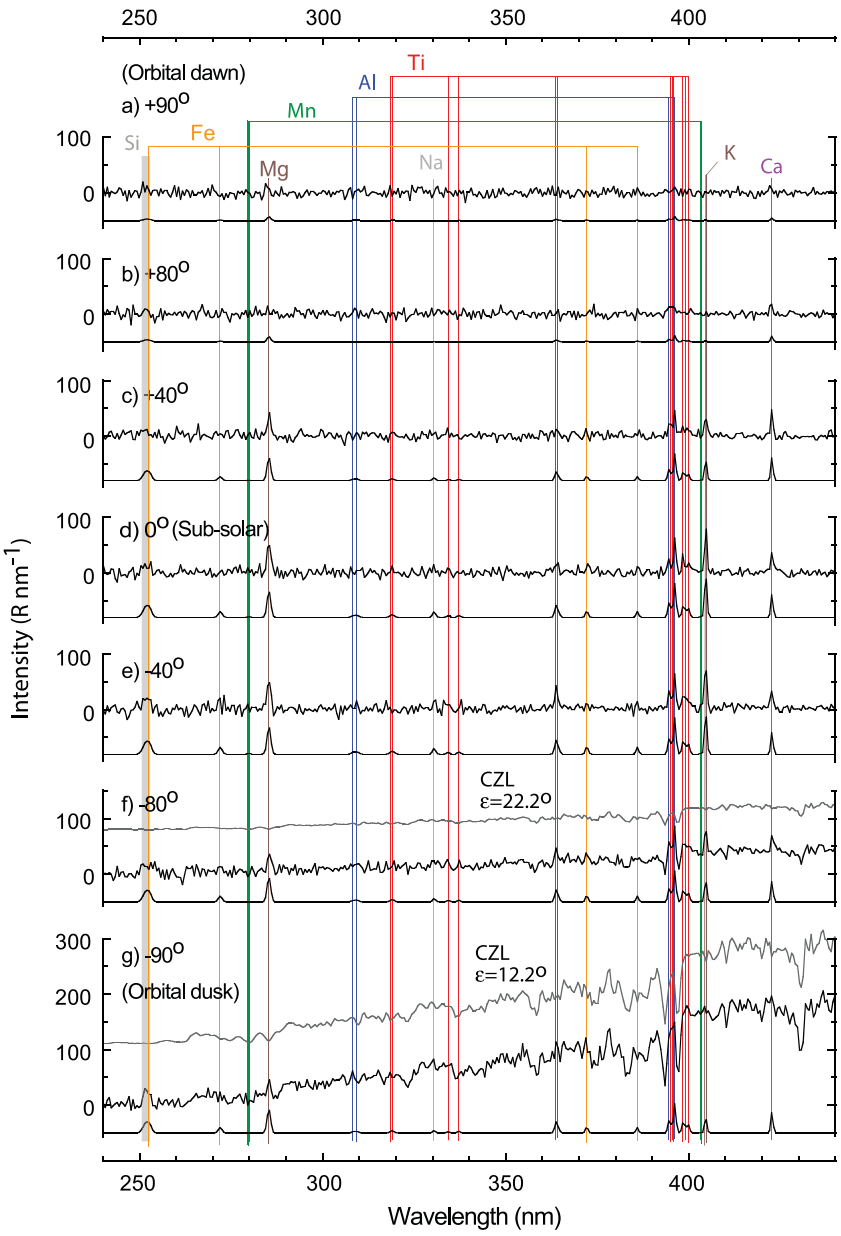

Figure 8. UVS simulations of spectral emission lines (240–440 nm) at solar azimuth positions along the LADEE orbital ground track, when the Moon is simultaneously exposed to micrometeoroids and the solar wind. Integration time = 100 s. The simulations were produced by spectrally convolving line intensity predictions shown in Figure 7 with a Gaussian blur function that has a wavelength-dependent width and with expected instrument noise levels, as described in the text. Presently, the noise-equivalent-radiance of LADEE UVS is not accurately determined shortward of ~300 nm, hence our simulations in this spectral region are based on an extrapolation of the instrument calibration above 300 nm. Noise free spectra are located below each simulation. With the exception of strong single features from Mg and Ca, observed emission features are typically the combined intensities of line multiplets with average spacing smaller than UVS resolution, so they appear as broadened but easily observable features. A single broad (gray) band is used to represent the six modeled Si lines between 250.8 and 252.9 nm, all of which have comparable intensities. Coronal-zodiacal-light (CZL) is included in these simulations, but it contributes significantly only at longer wavelengths and small solar elongation angles, ε, as shown by noise-free CZL models in the last two orbital positions (Figures 8f and 8g).

the detection of lines at small solar elongation angles, but it diminishes to less than the instrument noise at most spacecraft positions on the dayside, and UVS spectra in that region can be coadded without such corrections (top panels).

[51] According to our simulations, detections are strictly controlled by the UVS characteristics (noise and spectral resolution) at the levels predicted when the Moon is exposed to both micrometeoroids and the solar wind (≤50 R). For

Table 5. LADEE UVS Spectral Parameters That Were Assumed in Our Simulations

Line	NER (R nm^{-1})	$\Delta\lambda$ (nm)
Si 2515	67	1.27
Fe 2719	61	1.21
Mg 2852	55	1.16
Ti 3636	46	0.82
Fe 3720	45	0.76
Al 3962	37	0.72
Ca 4227	34	0.70

lines that lie in the low-noise portion of the UVS range (>300 nm), emission of ~30 R is resolvable with exposures lasting a minute or less. Some of the Fe lines and the main Si and Mg lines may be more difficult to observe than assumed here because of higher UVS noise levels at small wavelengths. Many Si lines are blended by the instrument resolution, which increases the chances of detection. The chance of Mn detection is very low (<1 R predicted). Our models suggest that, besides Na and K, short UVS exposures will most strongly constrain the production, loss and spatial distribution of Al, Ca, and Mg, which could be detectable over half the dayside with ≤60 s integration. With $\tau \approx 60$ s, Ti, Fe, and Si, in that order, may be detectable over a limited area of the dayside when the tangent point lies approximately over the subsolar point. Such brief integrations will determine the spatial distribution of neutrals with longitude resolution of ~3°, enabling us to distinguish among the physical processes that result in particle release.

[52] Finally, it is pertinent to ask: what if our exospheric abundances are overly optimistic? An estimate of the signal-to-noise ratio, *SNR*, at different integration times, τ (sec), may be obtained as

$$\mathrm{SNR} = \sqrt{\tau} \times (\mathrm{Line\_Intensity}(R)/\Delta\lambda)/\mathrm{NER}\ (1\ \mathrm{s}), \qquad (7)$$

where $\Delta\lambda$ is the UVS spectral resolution. Scaled-down versions of the impact models were used to compute the exposure time required to achieve a signal-to-noise ratio of four given the spectral resolution and the assumed NER at each line (Table 5). These calculations are summarized in Figure 9, where bars corresponding to the same low-altitude density across species illustrate that the ease of detection is a function of g value and instrument sensitivity. This approach identifies the lowest possible detection limits during the duration of the mission, and underlines the extent to which we can separately constrain contributions by impacts and sputtering by analyzing data obtained when the solar wind is shielded by Earth's magnetosphere. For this calculation science operations for 60 days with a 40% duty cycle for UVS were assumed. These conservative calculations prove that UVS can detect regolith-derived exospheric species at levels at least ten times less than our impact models suggest if spectra from the whole mission are coadded. Ca can be easily detected at levels more than 2 orders of magnitude less than present limits.

5. Summary

[53] A model that simulates the release processes of micrometeoroid impact vaporization, solar wind sputtering, and photon–stimulated desorption (for Na and K), was used to evaluate abundances for a number of exospheric species originating from the lunar regolith. Our simulations suggest the following:

[54] 1. The observed nonstoichiometry of exospheric refractories compared to Na and K levels is mainly attributed to photon-stimulated desorption of alkalis, and possibly evidence that Na does not stick to the surface on impact.

[55] 2. Available observations often do not constrain models. For instance, published limits for Mg, Fe, Al, and O are comparable to or much exceed the levels that can be provided by the combined action of meteoroids and the solar wind (Table 2 and Figure 7).

[56] 3. Modeled Si and Ti column abundances are higher than published limits by factors of 4 and 6, respectively, which may be related to our finding that the Si (3906 Å) and Ti (5036 Å) lines, probed from the ground by *Flynn and Stern* [1996], corresponded to excited states that are unlikely to be populated. A revision of those values may be necessary.

[57] 4. The Ca abundance we calculate is much higher than the upper limit, a result that we interpret as evidence of loss processes beyond those due to ballistic escape, adsorption, and photoionization. A similar overestimate of the expected Ca brightness was given by the model of *Morgan and Killen* [1997]. In our model Ca is found to be 40 times less abundant than the modeled levels due to impacts, implying losses to a stable molecule or its condensation from gas to solid states in the vapor cloud with efficiency exceeding 90% [*Berezhnoy*, 2010]. Furthermore, Ca is present at quantities below those predicted by the sputtered component, which implies that the effective sputtering yield for neutral Ca is

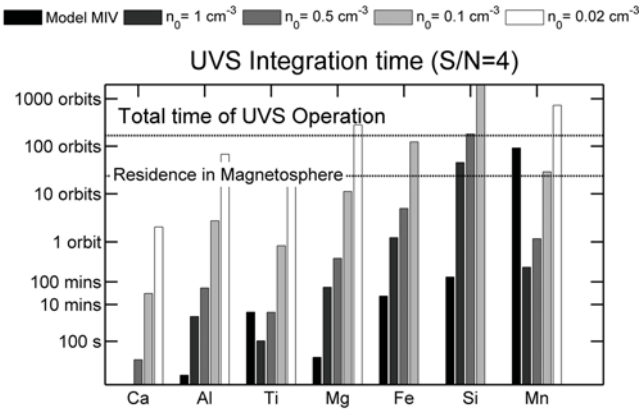

Figure 9. Estimated exposure time required to achieve a UVS signal-to-noise ratio (S/N) of four as a function of assumed low-altitude abundance. The effective operational time of LADEE UVS was estimated assuming 60 days of science operations with a 40% duty cycle for UVS. Over the lifetime of the LADEE mission, levels at least 10 times less than our micrometeoritic impact vaporization (MIV) model abundances, and at least 100 less than present limits for Ca, can be detected by UVS. Limits on Si will be better than suggested here because of the blending of multiple Si lines by the instrument (Figure 8). Mn is not detectable at expected levels.

0.01 atoms per ion or less. Species with low ionization potential, such as Ca, Na, K, and Al, may be sputtered off as ions at the expense of lower neutral sputtering yields [*Elphic et al.*, 1991; *Dukes et al.*, 2011]. Isotopic ratios of Ca in lunar grains are inconsistent with sputtering [*Kerridge and Kaplan*, 1978].

[58] Using this model, we simulated LADEE measurements for these species with the expectation that deviations between the model and LADEE data will constrain microphysical parameters such as the assumed sputtering yields, the degree of formation of condensates and molecular constituents, and the energy exchange with the surface. At the levels predicted by our model, and assuming simplified instrument characteristics and performance, O and Si from nominal impact rates as well as Na from PSD should be at the NMS detectability level. If confirmed, this means that approximately a factor of 3 to 4 enhancements of impact vapor during meteor streams (for O and Si) should yield detectable signals if O and Si produced by impacts are coming off as neutral atoms. Sodium should also be detectable by NMS just before the arrival of a solar storm due to increased UV by solar flares, and also during solar storms if the PSD efficiency for Na is enhanced twofold by increased solar wind precipitation [e.g., *Sarantos et al.*, 2010]. The detection of possible colder ejecta is strictly controlled by the instrument sensitivity to incoming atoms in the 0.2–0.5 eV energy range. The exact energy characteristic of the instrument will be measured during calibration. We finally predict that cold O at levels of 40 atoms cm^{-3} and S at levels of 20 atoms cm^{-3} can be detected with a signal-to-noise of two by NMS. Oxygen and sulphur can be constrained only by NMS because they emit outside the spectral range of the UVS.

[59] Our simulations for LADEE UVS, based on the assumption of equatorial sightlines pointing aft and having low-altitude tangent points (10–40 km), demonstrate that Na and K will be observed throughout the dayside with high signal-to-noise ratio except near the terminator, where Coronal-Zodiacal Light (CZL) and sunlight scattered by exospheric dust dominate [*Stubbs et al.*, 2010]. While the influence of exospheric dust away from the terminator is presently unknown, the effect of CZL on line emission was shown to be negligible for spacecraft locations up to $\pm 60^\circ$ from the subsolar point; therefore short exposures can be co-added without CZL removal over extensive regions of the dayside. Modeled emission levels for other species in the UVS spectral range were convolved to UVS resolution with Gaussian noise added at about the level anticipated for UVS. All species but Mn would be detectable with short ($\sim$1 min) integrations over limited areas of the dayside at levels predicted from impacts and sputtering, especially during times of Coronal Mass Ejections. Given the unknown magnitude of sources and losses, lower column abundances were simulated in order to show that, if spectra from several dayside passes are coadded, Al, Ca, Mg, and Ti at exospheric densities exceeding 0.02 atoms cm^{-3} near the surface, and Si and Fe at densities exceeding 0.5 atoms cm^{-3}, will be detectable with sufficient signal-to-noise ratio (S/N = 4). Detectable levels are 1 order of magnitude below published limits for Ti, more than 2 orders of magnitude below Ca limits, and at least 1 order of magnitude below nominal impact-driven models for other species (Table 2).

Appendix A: Notes on the Impact Vaporization Code

[60] The impact vapor code is described in section 3 of Morgan and Killen [1998].

[61] The equations used to describe theoretically the vaporization of the lunar surface are adopted for the planar impact approximation from *Melosh* [1989], equations 3.4.1 through 3.4.8 and equations 4.5.2 through 4.5.7. These equations describe the shock pressures in front and behind the shock, the compressed and uncompressed densities, velocities and internal specific energies derived from conservation of mass, momentum and energy across the discontinuity. Pressures for shock-induced vaporization and melting are given in the work of *Melosh* [1989, p. 44, Table 3.3], for onset and complete melting and vaporization, respectively, as a function of the target and impactor material. Although various materials can be input into the code (iron, aluminum, diabase, sandstone, dry sand, dunite), aluminum impactors are chosen as a proxy to stony-rich meteorites.

[62] Two other input parameters to the model are the delivery rate and velocity distribution of micrometeoroids. We assumed a mass per unit volume of meteoritic material near Earth of 3×10^{-16} g cm^{-3} for particles smaller than 1 cm [*Love and Brownlee*, 1993]. We used equation A8 from *Cintala* [1992] for the velocity distribution of micrometeors at the Moon and we assumed that mass and velocity are decoupled.

[63] **Acknowledgments.** NSO/Kitt Peak FTS data used here were produced by NSF/NOAO. G_values were computed using the oscillator strengths in the National Institute of Standards and Technology (NIST) online atomic database [*Ralchenko et al.*, 2010]. MS, RMK, DG, and TS acknowledge funding from the NASA Lunar Science Institute, DREAM. Additional funding for Stubbs, Glenar, and Killen was provided by NASA grant NNX09A079G (LASER). The authors thank Anthony Colaprete for providing results from the latest tests of the LADEE UVS performance. Two anonymous reviewers greatly improved the content of this paper with their comments.

[64] Masaki Fujimoto thanks the reviewers for their assistance in evaluating this paper.

References

Aumayr, F., and H. Winter (2004), Potential sputtering, *Philos. Trans. R. Soc. London A*, *362*, 77–102, doi:10.1098/rsta.2003.1300.

Berezhnoy, A. A. (2010), Meteoroid bombardment as a source of the lunar exosphere, *Adv. Space Res.*, *45*, 70–76, doi:10.1016/j.asr.2009.07.014.

Berezhnoy, A. A., and B. A. Klumov (2008), Impacts as sources of the exosphere on Mercury, *Icarus*, *195*, 511–522, doi:10.1016/j.icarus.2008.01.005.

Bruno, M., G. Cremonese, and S. Marchi (2006), Neutral sodium atoms release from the surface of the Moon induced by meteoroid impacts, *Mon. Not. R. Astron. Soc.*, *367*, 1067–1071, doi:10.1111/j.1365-2966.2006.10029.x.

Burger, M. H., R. M. Killen, R. J. Vervack Jr., E. T. Bradley, W. E. McClintock, M. Sarantos, M. Benna, and N. Mouawad (2010), Monte Carlo modeling of sodium in Mercury's exosphere during the first two MESSENGER flybys, *Icarus*, *209*, 63–74, doi:10.1016/j.icarus.2010.05.007.

Cassidy, T. A., and R. E. Johnson (2005), Monte Carlo model of sputtering and other ejection processes within a regolith, *Icarus*, *176*, 499–507, doi:10.1016/j.icarus.2005.02.013.

Chamberlain, J. W. (1963), Planetary coronae and atmospheric evaporation, *Planet. Space Sci.*, *11*, 901–960, doi:10.1016/0032-0633(63)90122-3.

Chamberlain, J. W., and D. M. Hunten (1987), *Theory of Planetary Atmospheres*, 291 pp., Academic, San Diego, Calif.

Cintala, M. E. (1992), Impact-induced thermal effects in the lunar and mercurian regoliths, *J. Geophys. Res.*, *97*, 947–973, doi:10.1029/91JE02207.

Delory, G. T., R. Elphic, T. Morgan, T. Colaprete, M. Horanyi, P. Mahaffy, B. Hine, and D. Boroson (2009), The Lunar Atmosphere and Dust Environment Explorer (LADEE), paper presented at 40th Lunar and Planetary Science Conference, (Lunar and Planetary Science XL), Lunar and Planet. Sci. Inst., The Woodlands, Tex., March 23–27.

Domingue, D., P. L. Koehn, R. M. Killen, A. L. Sprague, M. Sarantos, A. F. Cheng, E. T. Bradley, and W. E. McClintock (2007), Mercury's surface bounded exosphere, *Space Sci. Rev.*, *131*, 161–186, doi:10.1007/s11214-007-9260-9.

Dukes, C. A., W. Y. Chang, M. Famá, and R. A. Baragiola (2011), Laboratory studies on the sputtering contribution to the sodium atmospheres of Mercury and the Moon, *Icarus*, *212*, 463–469, doi:10.1016/j.icarus.2011.01.027.

Eichhorn, G. (1978), Heating and vaporization during hypervelocity particle impact, *Planet. Space Sci.*, *26*, 463–467, doi:10.1016/0032-0633(78)90067-3.

Elphic, R. C., H. O. Funsten, B. L. Barraclough, D. J. McComas, M. T. Paffet, D. T. Vaniman, and G. Heiken (1991), Lunar surface composition and solar wind–induced secondary ion mass spectrometry, *Geophys. Res. Lett.*, *18*, 2165–2168, doi:10.1029/91GL02669.

Ennico, K., A. Colaprete, M. Shirley, and D. Wooden (2010), Lunar Crater Observation and Sensing Satellite (LCROSS) Instrument Calibration Summary, ftp://pdsimage2.wr.usgs.gov/cdroms/LCROSS/lcro_0001/calib/calrpt.pdf, NASA Planet. Data Syst., Greenbelt, Md.

Ennico, K., M. Shirley, A. Colaprete, and L. Osetinsky (2012), The Lunar Crater Observation and Sensing Satellite (LCROSS) Payload development and performance in flight [online], *Space Sci. Rev.*, doi:10.1007/s11214-011-9753-4, in press.

Fastie, W. G., P. D. Feldman, R. C. Henry, H. W. Moos, C. A. Barth, G. E. Thomas, and T. M. Donahue (1973), A search for far-ultraviolet emissions from the lunar atmosphere, *Science*, *182*, 710–711, doi:10.1126/science.182.4113.710.

Feldman, P. D., and D. Morrison (1991), The Apollo 17 Ultraviolet Spectrometer: Lunar atmosphere measurements revisited, *Geophys. Res. Lett.*, *18*, 2105–2108, doi:10.1029/91GL01998.

Flynn, B. C., and S. A. Stern (1996), A spectroscopic survey of metallic species abundances in the lunar atmosphere, *Icarus*, *124*, 530–536, doi:10.1006/icar.1996.0228.

Georgiev, G., D. A. Glenar, and J. J. Hillman (2002), Spectral characterization of acousto-optic filters used in imaging spectroscopy, *Appl. Opt.*, *41*, 209–217, doi:10.1364/AO.41.000209.

Hahn, J. M., H. A. Zook, B. Cooper, and B. Sunkara (2002), Clementine observations of the zodiacal light and the dust content of the inner solar system, *Icarus*, *158*, 360–378, doi:10.1006/icar.2002.6881.

Hartle, R. E. (1971), Model for rotating and nonuniform planetary exospheres, *Phys. Fluids*, *14*, 2592–2598, doi:10.1063/1.1693379.

Heiken, G. H., D. T. Vaniman, and B. M. French (1991), *Lunar Sourcebook—A User's Guide to the Moon*, Cambridge Univ. Press, New York.

Hilchenbach, M., D. Hovestadt, B. Klecker, and E. Moebius (1992), Detection of singly ionized energetic lunar pick-up ions upstream of Earth's bow shock, in *Solar Wind Seven; Proceedings of the 3rd COSPAR Colloquium, Goslar, Germany, Sept. 16–20, 1991*, *COSPAR Colloq. Ser.*, vol. 3, edited by E. Marsch and R. Schwenn, pp. 349–355, Pergamon, Elmsford, N. Y.

Kerridge, J. F., and I. R. Kaplan (1978), Sputtering: Its relationship to isotopic fractionation on the lunar surface, in *Proceedings of the Ninth Lunar and Planetary Science Conference, Houston, Texas, March 13–17*, pp. 1687–1709, Pergamon, New York.

Killen, R. M., T. A. Bida, and T. H. Morgan (2005), The calcium exosphere of Mercury, *Icarus*, *173*, 300–311, doi:10.1016/j.icarus.2004.08.022.

Killen, R. M., et al. (2007), Processes that promote and deplete the atmosphere of Mercury, *Space Sci. Rev.*, *132*, 433–509, doi:10.1007/s11214-007-9232-0.

Killen, R. M., D. Shemansky, and N. Mouawad (2009), Expected emission from Mercury's exospheric species, and their ultraviolet-visible signatures, *Astrophys. J. Suppl. Ser.*, *181*, 351–359, doi:10.1088/0067-0049/181/2/351.

Killen, R. M., A. E. Potter, R. J. Vervack Jr., E. T. Bradley, W. E. McClintock, and C. M. Anderson (2010), Observations of metallic species in Mercury's exosphere, *Icarus*, *209*, 75–87, doi:10.1016/j.icarus.2010.02.018.

Kurucz, R. L., I. Furenlid, J. Brault, and L. Testerman (1984), *Solar Flux Atlas From 296 to 1300 nm*, Natl. Solar Obs., Sunspot, N. M.

Leinert, C., et al. (1998), The 1997 reference of diffuse sky brightness, *Astron. Astrophys. Suppl. Ser.*, *127*, 1–99, doi:10.1051/aas:1998105.

Love, S. G., and D. E. Brownlee (1993), A direct measurement of the terrestrial mass accretion rate of cosmic dust, *Science*, *262*, 550–553, doi:10.1126/science.262.5133.550.

Macqueen, R. M., C. L. Ross, and T. Mattingly (1973), Observations from space of the solar corona/inner zodiacal light, *Planet. Space Sci.*, *21*, 2173–2179, doi:10.1016/0032-0633(73)90191-8.

Madey, T. E., B. V. Yakshinskiy, V. N. Ageev, and R. E. Johnson (1998), Desorption of alkali atoms and ions from oxide surfaces: Relevance to origins of Na and K in the atmospheres of Mercury and the Moon, *J. Geophys. Res.*, *103*, 5873–5887, doi:10.1029/98JE00230.

Mall, U., E. Kirsch, K. Cierpka, B. Wilken, A. Söding, F. Neubauer, G. Gloeckler, and A. Galvin (1998), Direct observation of lunar pick-up ions near the Moon, *Geophys. Res. Lett.*, *25*, 3799–3802, doi:10.1029/1998GL900003.

McClintock, W. E., R. J. Vervack Jr., E. T. Bradley, R. M. Killen, N. Mouawad, A. L. Sprague, M. H. Burger, S. C. Solomon, and N. R. Izenberg (2009), MESSENGER observations of Mercury's exosphere: Detection of magnesium and distribution of constituents, *Science*, *324*, 610–613.

Melosh, H. J. (1989), *Impact Cratering: A Geologic Process*, *Oxford Monogr. Geol. Geophys. Ser.*, Oxford Univ. Press, Oxford, U. K.

Meyer, F. W., P. R. Harris, C. N. Taylor, H. M. Meyer III, A. F. Barghouty, and J. H. Adams (2011), Sputtering of lunar regolith simulant by protons and singly and multicharged Ar ions at solar wind energies, *Nucl. Inst. Methods Phys. Res. B*, *269*, 1316–1620, doi:10.1016/j.nimb.2010.11.091.

Morgan, T. H., and R. M. Killen (1997), A non-stoichiometric model of the composition of the atmospheres of Mercury and the Moon, *Planet. Space Sci.*, *45*, 81–94, doi:10.1016/S0032-0633(96)00099-2.

Morgan, T. H., and R. M. Killen (1998), Production mechanisms for faint but possibly detectable coronae about asteroids, *Planet. Space Sci.*, *46*, 843–850, doi:10.1016/S0032-0633(98)00029-4.

Mouawad, N., M. H. Burger, R. M. Killen, A. E. Potter, S. Naidu, W. E. McClintock, R. J. Vervack Jr., and E. T. Bardley (2011), Constraints on Mercury's sodium exosphere: Combined MESSENGER and ground-based data, *Icarus*, *211*, 21–36, doi:10.1016/j.icarus.2010.10.019.

Mura, A., P. Wurz, H. I. M. Lichtenegger, H. Schleicher, H. Lammer, D. Delcourt, A. Millilo, S. Orsini, S. Massetti, and M. L. Khodachenko (2009), The sodium exosphere of Mercury: Comparison between observations during Mercury's transit and model results, *Icarus*, *200*, 1–11, doi:10.1016/j.icarus.2008.11.014.

Papike, J. J., S. B. Simon, and J. C. Laul (1982), The lunar regolith: Chemistry, mineralogy, and petrology, *Rev. Geophys.*, *20*, 761–826, doi:10.1029/RG020i004p00761.

Pitz, E., C. Leinhart, A. Schulz, and H. Link (1979), Colour and polarization of the zodiacal light from the ultraviolet to the near infrared, *Astron. Astrophys.*, *74*, 15–20.

Potter, A. E., and T. H. Morgan (1988), Discovery of sodium and potassium vapor in the atmosphere of the Moon, *Science*, *241*, 675–680, doi:10.1126/science.241.4866.675.

Ralchenko, Y., et al. (2010), NIST Atomic Spectra Database, http://physics.nist.gov/asd, Natl. Inst. Stand. Tech., Gaithersburg, Md.

Saito, Y., et al. (2010), In-flight performance and initial results of Plasma Energy Angle and Composition Experiment (PACE) on SELENE (Kaguya), *Space Sci. Rev.*, *154*, 265–303, doi:10.1007/s11214-010-9647-x.

Sarantos, M., R. M. Killen, A. S. Sharma, and J. A. Slavin (2010), Sources of sodium in the lunar exosphere: Modeling using ground-based observations and spacecraft data of the plasma, *Icarus*, *205*, 364–374, doi:10.1016/j.icarus.2009.07.039.

Sarantos, M., R. M. Killen, W. E. McClintock, E. T. Bradley, R. J. Vervack Jr., M. Benna, and J. A. Slavin (2011), Limits to Mercury's magnesium exosphere from MESSENGER second flyby observations, *Planet. Space Sci.*, *59*, 1992–2003, doi:10.1016/j.pss.2011.05.002.

Stern, S. A. (1999), The lunar atmosphere: History, status, current problems, and context, *Rev. Geophys.*, *37*, 453–491, doi:10.1029/1999RG900005.

Stern, S. A., J. W. Parker, T. H. Morgan, B. C. Flynn, D. M. Hunten, A. Sprague, M. Mendillo, and M. C. Festou (1997), An HST search for magnesium in the lunar atmosphere, *Icarus*, *127*, 523–526, doi:10.1006/icar.1997.5716.

Stubbs, T. J., D. A. Glenar, A. Colaprete, and D. T. Richard (2010), Optical scattering processes observed at the Moon: Predictions for the LADEE ultraviolet spectrometer, *Planet. Space Sci.*, *58*, 830–837, doi:10.1016/j.pss.2010.01.002.

Tanaka, T., et al. (2009), First in situ observation of the Moon-originating ions in the Earth's Magnetosphere by MAP-PACE on SELENE (KAGUYA), *Geophys. Res. Lett.*, *36*, L22106, doi:10.1029/2009GL040682.

Verner, D. A., G. J. Ferland, K. T. Korista, and D. G. Yakovlev (1996), Atomic data for astrophysics. II. New analytic FITS for photoionization

cross sections of atoms and ions, *Astrophys. J.*, *465*, 487–498, doi:10.1086/177435.

Waite, J. H., et al. (2004), The Cassini Ion and Neutral Mass Spectrometer (INMS) investigation, *Space Sci. Rev.*, *114*, 113–231, doi:10.1007/s11214-004-1408-2.

Wurz, P., U. Rohner, J. A. Whitby, C. Kolb, H. Lammer, P. Dobnikar, and J. A. Martín-Fernández (2007), The lunar exosphere: The sputtering contribution, *Icarus*, *191*, 486–496, doi:10.1016/j.icarus.2007.04.034.

Wurz, P., J. A. Whitby, U. Rohner, J. A. Martín-Fernández, H. Lammer, and C. Kolb (2010), Self-consistent modelling of Mercury's exosphere by sputtering, micro-meteorite impact and photon-stimulated desorption, *Planet. Space Sci.*, *58*, 1599–1616, doi:10.1016/j.pss.2010.08.003.

Yakshinskiy, B. V., and T. E. Madey (1999), Photon-stimulated desorption as a substantial source of sodium in the lunar atmosphere, *Nature*, *400*, 642–644, doi:10.1038/23204.

Yakshinskiy, B. V., and T. E. Madey (2005), Temperature-dependent DIET of alkalis from SiO_2 films: Comparison with a lunar sample, *Surf. Sci.*, *593*, 202–209, doi:10.1016/j.susc.2005.06.062.

Yokota, S., et al. (2009), First direct detection of ions originating from the Moon by MAP-PACE IMA onboard SELENE (KAGUYA), *Geophys. Res. Lett.*, *36*, L11201, doi:10.1029/2009GL038185.

M. Benna, Solar System Exploration Division, NASA Goddard Space Flight Center, 8800 Greenbelt Rd., Greenbelt, MD 20771, USA.

D. A. Glenar, Astronomy Department, New Mexico State University, Box 30001/MSC4500, Las Cruces, NM 88003, USA.

R. M. Killen, Planetary Magnetospheres Branch, NASA Goddard Space Flight Center, Mail Code 695, Greenbelt, MD 20771, USA.

M. Sarantos, Heliophysics Science Division, NASA Goddard Space Flight Center, Building 21, Room C222, Greenbelt, MD 20771, USA. (menelaos.sarantos-1@nasa.gov)

T. J. Stubbs, Solar System Exploration Division, NASA Goddard Space Flight Center, Mail Code 695, Greenbelt, MD 20771, USA.